

Event patterns extracted from transverse momentum and rapidity spectra of Z bosons and quarkonium states produced in pp and Pb-Pb collisions at LHC

Ya-Hui Chen^a, Fu-Hu Liu^{a,1}, and Roy A. Lacey^{b,2}

^a*Institute of Theoretical Physics, Shanxi University, Taiyuan, Shanxi 030006, China*

^b*Departments of Chemistry & Physics, Stony Brook University, Stony Brook, NY 11794, USA*

Abstract: Transverse momentum (p_T) and rapidity (y) spectra of Z bosons produced in proton-proton (pp) and lead-lead (Pb-Pb) collisions, and quarkonium states [charmonium $c\bar{c}$ mesons J/ψ and $\psi(2S)$, and bottomonium $b\bar{b}$ mesons $\Upsilon(1S)$, $\Upsilon(2S)$, and $\Upsilon(3S)$] produced in pp collisions, at the large hadron collider (LHC) are uniformly described by a hybrid model of two-component Erlang distribution for p_T spectrum and Gaussian distribution for y spectrum. The former distribution results from a multisource thermal model, and the latter one results from the Landau hydrodynamic model and its revision. The modelling results are in agreement with the experimental data of the CMS, ALICE, and LHCb Collaborations measured in pp collisions at center-of-mass energy $\sqrt{s} = 2.76$ and 7 TeV, and in Pb-Pb collisions at center-of-mass energy per nucleon pair $\sqrt{s_{NN}} = 2.76$ TeV. Based on the parameter values extracted from p_T and y spectra, the event patterns in two-dimensional p_T - y space and in three-dimensional velocity space are obtained.

Keywords: Transverse momentum spectrum, rapidity spectrum, event pattern

PACS: 12.38.Mh, 25.75.Dw, 24.10.Pa

1 Introduction

High energy nucleus-nucleus collisions at the relativistic heavy ion collider (RHIC) and large hadron collider (LHC) [1–4] provide excellent environment and condition of high temperature and density, where a new state of matter, namely the quark-gluon plasma (QGP) [5, 6], is expected to form and to live for a very short lifetime. It is regretful that the QGP cannot be directly measured in experiments due to its very short lifetime. Instead, to understand the formation and properties of QGP, the distribution laws of final-state particles are studied. However, experiments are complex and difficult, which render that the quantities measured in experiments are limited. To analyze more information from limited experimental quantities is necessary.

Generally, interacting system in nucleus-nucleus collisions undergoes a few stages which include, but are not limited to, the scattering, color glass condensate, thermalization, hadronization, chemical equilibrium and freeze-out, kinetic equilibrium and freeze-out. The distribution laws of final-state particle transverse momenta and rapidities reflect

¹E-mail: fuhuliu@163.com; fuhuliu@sxu.edu.cn

²E-mail: Roy.Lacey@Stonybrook.edu

the situation of interacting system at the stage of kinetic freeze-out, while the ratios of different particles reflect the situation at the stage of chemical freeze-out. Based on descriptions of transverse momentum (p_T) and rapidity (y) spectra, one can extract some information of transverse excitation and longitudinal extension of interacting system. Thus, other information such as the event pattern in two-dimensional p_T - y space and three-dimensional velocity space can be partly extracted from parameters fitted to p_T and y spectra [7, 8].

In peripheral nucleus-nucleus collisions, less nucleons take part in the interactions. The most peripheral nucleus-nucleus collisions contains only two nucleons, one is from the target and the other one is from the projectile. Proton-proton (pp) collisions are similar to the most peripheral nucleus-nucleus collisions in the case of neglecting the spectator (cold nuclear) effect. We are interested in both pp collisions and lead-lead (Pb-Pb) collisions at the LHC.

In this paper, based on a hybrid model of two-component Erlang distribution for p_T spectrum (which results from a multisource thermal model [9–11]) and Gaussian distribution for y spectrum (which results from the Landau hydrodynamic model and its revision [12–20]), we analyze together p_T and y spectra of Z bosons produced in pp collisions at center-of-mass energy $\sqrt{s} = 2.76$ TeV, and in Pb-Pb collisions at center-of-mass energy per nucleon pair $\sqrt{s_{NN}} = 2.76$ TeV. At the same time, p_T and y spectra of quarkonium states [charmonium $c\bar{c}$ mesons J/ψ and $\psi(2S)$, and bottomonium $b\bar{b}$ mesons $\Upsilon(1S)$, $\Upsilon(2S)$, and $\Upsilon(3S)$] produced in pp collisions at $\sqrt{s} = 7$ TeV are analyzed. The modelling results are in agreement with the experimental data of the CMS [21–23], ALICE [24–26], and LHCb Collaborations [27–29]. Based on the parameters extracted from p_T and y spectra, the event patterns at kinetic freeze-out in two-dimensional p_T - y space and in three-dimensional velocity space are obtained.

The structure of the present work is as followings. The model and method are shortly described in section 2. Results and discussion are given in section 3. In section 4, we summarize our main observations and conclusions.

2 The model and method

Firstly, we need modelling descriptions of p_T and y spectra. In the framework of multisource thermal model [9–11], we can obtain an Erlang distribution or a two-, three- or multi-component Erlang distribution to fit p_T spectrum. According to the model, many (m) emission sources stayed at the same excitation state are assumed to form in high energy collisions. Each (the i -th) source is assumed to contribute to transverse momentum p_{Ti} by an exponential function

$$f_{p_{Ti}}(p_{Ti}) = \frac{1}{\langle p_{Ti} \rangle} \exp\left(-\frac{p_{Ti}}{\langle p_{Ti} \rangle}\right), \quad (1)$$

where $\langle p_{Ti} \rangle$ denotes the average value of p_{Ti} , which results in Eq. (1) to be a probability distribution and $\int_0^\infty f_{p_{Ti}}(p_{Ti}) dp_{Ti} = 1$.

The m sources which contribute to p_T result in an Erlang distribution [11]

$$f_{p_T}(p_T) = \frac{p_T^{m-1}}{(m-1)!\langle p_{Ti} \rangle^m} \exp\left(-\frac{p_T}{\langle p_{Ti} \rangle}\right) \quad (2)$$

which is the folding of m exponential distributions. In the case of considering two-component Erlang distribution, we have

$$f_{p_T}(p_T) = \frac{k_1 p_T^{m_1-1}}{(m_1-1)! \langle p_{Ti} \rangle_1^{m_1}} \exp\left(-\frac{p_T}{\langle p_{Ti} \rangle_1}\right) + \frac{(1-k_1) p_T^{m_2-1}}{(m_2-1)! \langle p_{Ti} \rangle_2^{m_2}} \exp\left(-\frac{p_T}{\langle p_{Ti} \rangle_2}\right), \quad (3)$$

where k_1 denotes the relative contribution of the first component, and the subscripts 1 and 2 denote the quantities related to the first and second components respectively. Eqs. (2) and (3) are also probability distributions which are normalized to 1. When we compare them with experimental data, normalization constant (N_{p_T}) which is used to fit the data is needed.

On y spectrum, we choose the Landau hydrodynamic model and its revision [12–20]. In the model, the interacting system is described by the hydrodynamics. The y spectrum can be described by a Gaussian function [19, 20]

$$f_y(y) = \frac{1}{\sqrt{2\pi}\sigma_y} \exp\left[-\frac{(y-y_C)^2}{2\sigma_y^2}\right], \quad (4)$$

where σ_y denotes the rapidity distribution width and y_C denotes the mid-rapidity. In symmetric collisions, $y_C = 0$ in the center-of-mass reference frame. As a probability distribution, Eq. (4) is normalized to 1. When we compare it with experimental data, a normalization constant (N_y) which is used to fit the data is needed.

Secondly, we need discrete values of p_T and y , as well as other quantities. The related calculation is performed by a Monte Carlo method. Let r_i , r_{1i} , r_{2i} , and $R_{1,2}$ denote random numbers in $[0,1]$. Eqs. (2)–(4) results in

$$p_T = -\langle p_{Ti} \rangle \sum_{i=1}^m r_i, \quad (5)$$

$$p_T = -\langle p_{Ti} \rangle_1 \sum_{i=1}^{m_1} r_{1i} \quad (6)$$

for the first component, or

$$p_T = -\langle p_{Ti} \rangle_2 \sum_{i=1}^{m_2} r_{2i} \quad (7)$$

for the second component, and

$$y = \sigma_y \sqrt{-2 \ln R_1} \cos(2\pi R_2) + y_C, \quad (8)$$

respectively.

The energy E is given by

$$E = \sqrt{p^2 + m_0^2}. \quad (9)$$

The x - and y -components of p_T are given by

$$p_x = p_T \cos \varphi, \quad p_y = p_T \sin \varphi \quad (10)$$

respectively, where φ is the azimuthal angle to distribute evenly in $[0, 2\pi]$. Combining with Eqs. (9) and (10), we have the velocity

$$\beta = \frac{p}{E} \quad (11)$$

and its components

$$\beta_x = \frac{p_x}{E}, \quad \beta_y = \frac{p_y}{E}, \quad \beta_z = \frac{p_z}{E} \quad (12)$$

respectively. All velocity and its components are in the units of c which is the speed of light in vacuum and equals to 1 in natural units.

3 Results and discussion

Figure 1 presents (a)(b) transverse momentum spectra, $d^2\sigma/(dydp_T)$, and (c)(d) rapidity spectra, $d\sigma/dy$, of Z bosons produced in pp collisions at $\sqrt{s} = 2.76$ TeV for the (a)(c) dimuon ($\mu\mu$) and (b)(d) dielectron (ee) decay channels in $y < 2.0$ and $y < 1.44$ respectively, where σ in the longitudinal axis denotes the cross-section and the integral luminance $L_{\text{int}} = 5.4 \text{ pb}^{-1}$. The closed squares represent the experimental data of the CMS Collaboration [21], and the open squares are obtained by reflecting the data at $y = 0$. The curves are our results calculated by the two-component Erlang distribution for p_T spectra and Gaussian distribution for y spectra, which are the results of the multisource thermal model [9–11] and the Landau hydrodynamic model [12–20], respectively. In the calculation, the method of least squares is used to determine the values of parameters when we do the fit to experimental data. The values of free parameters ($m_1, \langle p_{Ti} \rangle_1, k_1, m_2, \langle p_{Ti} \rangle_2$, and σ_y), normalization constants (N_{p_T} and N_y), and χ^2 per degree of freedom (χ^2/dof) are listed in Tables 1 and 2, where the normalization constant N_{p_T} (or N_y) is used to give comparison between the normalized curve with experimental p_T (or y) spectrum. One can see that the results calculated by using the hybrid model are in agreement with the experimental data of Z bosons measured by the CMS Collaboration.

Figure 2 is similar to Figure 1, but it shows the results in minimum-bias (0–100% centrality) Pb-Pb collisions at $\sqrt{s_{NN}} = 2.76$ TeV, where N in the longitudinal axis denotes the number of particles and $L_{\text{int}} = 150 \mu\text{b}^{-1}$. The values of free parameters, normalization constants, and χ^2/dof are listed in Tables 1 and 2. Once again, the results calculated by using the hybrid model are in agreement with the experimental data of the CMS Collaboration.

Based on the parameter values obtained from Figures 1 and 2, we can perform a Monte Carlo calculation and obtain a series of kinematic quantities. For example, event patterns (particle scatter plots) in two-dimensional $p_T - y$ space are presented in Figure 3 for (a)(c) $Z \rightarrow \mu\mu$ and (b)(d) $Z \rightarrow ee$ channels in (a)(b) pp collisions at $\sqrt{s} = 2.76$ TeV and (c)(d) Pb-Pb collisions at $\sqrt{s_{NN}} = 2.76$ TeV. The total number of particles for each panel is 1000. The squares and circles represent the contributions of the first and second components in the two-component Erlang distribution respectively. Most particles appear in the region of low- p_T and low- y . The values of root-mean-squares ($\sqrt{\langle p_T^2 \rangle}$ for p_T and $\sqrt{\langle y^2 \rangle}$ for y) are listed in Table 3.

Figure 4 is another example of event pattern in three-dimensional velocity ($\beta_x - \beta_y - \beta_z$) space for (a)(c) $Z \rightarrow \mu\mu$ and (b)(d) $Z \rightarrow ee$ channels in (a)(b) pp collisions at $\sqrt{s} = 2.76$ TeV and (c)(d) Pb-Pb collisions at $\sqrt{s_{NN}} = 2.76$ TeV. The total number of particles for each panel is 1000. The red and blue globules represent the contributions of the first and second components in the two-component Erlang distribution respectively. Most particles appear in the region of low- β_x and low- β_y . The values of root-mean-squares ($\sqrt{\beta_x^2}$ for β_x , $\sqrt{\beta_y^2}$ for β_y , and $\sqrt{\beta_z^2}$ for β_z) and the maximum $|\beta_x|$, $|\beta_y|$, and $|\beta_z|$ ($|\beta_x|_{\max}$, $|\beta_y|_{\max}$, and $|\beta_z|_{\max}$) are listed in Table 4. One can see that $\sqrt{\beta_x^2} \approx \sqrt{\beta_y^2} \ll \sqrt{\beta_z^2}$, and $|\beta_x|_{\max} \approx |\beta_y|_{\max} < |\beta_z|_{\max}$. The event pattern in velocity (or coordinate) space looks like a rough cylinder along z axis (beam direction) when it emit Z bosons, and the maximum velocity surface (the surface consisted of the maximum velocities in different directions) is a fat cylinder.

In Figure 5, the spectra of inclusive (a) J/ψ p_T , (b) $\psi(2S)$ p_T , (c) J/ψ y , and (d) $\psi(2S)$ y in pp collisions at $\sqrt{s} = 7$ TeV are displayed. Different solid symbols represent different data measured by the ALICE [24–26] and LHCb collaborations [27, 28] in different conditions shown in the panels, and the open symbols are reflected at $y = 0$. The curves for p_T and y spectra are our results calculated by using the two-component Erlang distribution and Gaussian distribution respectively. The values of free parameters, normalization constants, and χ^2/dof are listed in Tables 1 and 2. One can see that the results calculated by using the hybrid model are in agreement with the experimental data of quarkonium states [charmonium $c\bar{c}$ mesons J/ψ and $\psi(2S)$] measured by the ALICE and LHCb Collaborations.

Based on the parameter values obtained from Figure 5, we can obtain some event patterns for charmonium $c\bar{c}$ mesons J/ψ and $\psi(2S)$. In Figures 6 and 7, the event patterns in $p_T - y$ and $\beta_x - \beta_y - \beta_z$ spaces for inclusive (a) J/ψ and (b) $\psi(2S)$ are given. The red squares and globules represent the contribution of the first component, and the blue circles and globules represent the contribution of the second component, in the two-component Erlang distribution. The corresponding values of root-mean squares and the maximum velocity components are listed in Tables 3 and 4. One can see that $\sqrt{p_T^2}$ for charmonium $c\bar{c}$ mesons is less than that for Z bosons, and $\sqrt{y^2}$ for the two types of particles are close to each other. Once again, $\sqrt{\beta_x^2} \approx \sqrt{\beta_y^2} \ll \sqrt{\beta_z^2}$, and $|\beta_x|_{\max} \approx |\beta_y|_{\max} < |\beta_z|_{\max}$. At the same time, $\sqrt{\beta_x^2}$ and $|\beta_x|_{\max}$ (or $\sqrt{\beta_y^2}$ and $|\beta_y|_{\max}$) for charmonium $c\bar{c}$ mesons are larger than those for Z bosons, and $\sqrt{\beta_z^2}$ and $|\beta_z|_{\max}$ are nearly the same severally for the two types of particles. The event pattern in velocity (or coordinate) space looks like a rough cylinder along beam direction when it emit charmonium $c\bar{c}$ mesons, and the maximum velocity surface is a fat cylinder.

In Figure 8, the spectra of (a) p_T for $\Upsilon(1S)$, $\Upsilon(2S)$, and $\Upsilon(3S)$, and (b) y for $\Upsilon(1S)$, $\Upsilon(2S)$, and $\Upsilon(3S)$ produced in pp collisions at $\sqrt{s} = 7$ TeV are presented. The sold circles, squares, and triangles represent the experimental data of $\Upsilon(1S)$, $\Upsilon(2S)$, and $\Upsilon(3S)$, respectively, measured by the LHCb Collaboration [29], and the open symbols are reflected at $y = 0$. The curves for p_T and y spectra are our results calculated by using the two-component Erlang distribution and Gaussian distribution respectively. The

values of free parameters, normalization constants, and χ^2/dof are listed in Tables 1 and 2. One can see that the results calculated by using the hybrid model are in agreement with the experimental data of quarkonium states [bottomonium $b\bar{b}$ mesons $\Upsilon(1S)$, $\Upsilon(2S)$, and $\Upsilon(3S)$] measured by the LHCb Collaboration.

To study further the y spectra of bottomonium $b\bar{b}$ mesons, Figures 9(a) and 9(b) give the results for $\Upsilon(1S)$ and $\Upsilon(2S)$ in pp collisions at 7 TeV respectively. Different solid symbols represent different data measured by the ALICE [24], LHCb [29], and CMS collaborations [22, 23] in different conditions shown in the panels, and the open symbols are reflected at $y = 0$. The values of free parameters, normalization constants, and χ^2/dof are listed in Table 2. One can see that the results calculated by using the Landau hydrodynamic model are in indeed agreement with the experimental data of bottomonium $b\bar{b}$ mesons $\Upsilon(1S)$ and $\Upsilon(2S)$.

Based on the parameter values obtained from Figure 8, we can obtain some event patterns for bottomonium $b\bar{b}$ mesons $\Upsilon(1S)$, $\Upsilon(2S)$, and $\Upsilon(3S)$. In Figures 10 and 11, the event patterns in $p_T - y$ and $\beta_x - \beta_y - \beta_z$ spaces for (a) $\Upsilon(1S)$, (b) $\Upsilon(2S)$, and (c) $\Upsilon(3S)$ are given. The red squares and globules represent the contribution of the first component, and the blue circles and globules represent the contribution of the second component, in the two-component Erlang distribution. The corresponding values of root-mean squares and the maximum velocity components are listed in Tables 3 and 4. One can see that $\sqrt{p_T^2}$ for bottomonium $b\bar{b}$ mesons is close to that for charmonium $c\bar{c}$ mesons, and less than that for Z bosons, while $\sqrt{y^2}$ for the three types of particles are close to each other. Once more, $\sqrt{\beta_x^2} \approx \sqrt{\beta_y^2} \ll \sqrt{\beta_z^2}$, and $|\beta_x|_{\text{max}} \approx |\beta_y|_{\text{max}} < |\beta_z|_{\text{max}}$. At the same time, $\sqrt{\beta_x^2}$ and $|\beta_x|_{\text{max}}$ (or $\sqrt{\beta_y^2}$ and $|\beta_y|_{\text{max}}$) for bottomonium $b\bar{b}$ mesons are larger than those for Z bosons, and both the quarkonium states correspond to nearly the same $\sqrt{\beta_x^2}$ and $|\beta_x|_{\text{max}}$ (or $\sqrt{\beta_y^2}$ and $|\beta_y|_{\text{max}}$). For the three types of particles, $\sqrt{\beta_z^2}$ and $|\beta_z|_{\text{max}}$ are nearly the same severally. The event pattern in velocity (or coordinate) space looks like a rough cylinder along beam direction when it emit bottomonium $b\bar{b}$ mesons, and the maximum velocity surface is a fat cylinder.

4 Conclusions

We summarize here our main observations and conclusions.

(a) The transverse momentum and rapidity spectra of Z bosons produced in pp and Pb-Pb collisions at 2.76 TeV, and the same spectra of charmonium $c\bar{c}$ mesons [J/ψ and $\psi(2S)$] and bottomonium $b\bar{b}$ mesons [$\Upsilon(1S)$, $\Upsilon(2S)$, and $\Upsilon(3S)$] produced in pp collisions at 7 TeV at the LHC are uniformly described by the hybrid model of two-component Erlang distribution for p_T spectrum and Gaussian distribution for y spectrum. The former distribution results from the multisource thermal model, and the later one results from the Landau hydrodynamics model. The modelling results are in agreement with the experimental data of the CMS, ALICE, and LHCb Collaborations

(b) Based on the parameter values extracted from p_T and y spectra, the event patterns (or particle scatter plots) in two-dimensional p_T - y space and in three-dimensional velocity

(or coordinate) space are obtained. In particular, $\sqrt{\beta_x^2} \approx \sqrt{\beta_y^2} \ll \sqrt{\beta_z^2}$, and $|\beta_x|_{\max} \approx |\beta_y|_{\max} < |\beta_z|_{\max}$, which renders that the event pattern in velocity (or coordinate) space looks like a rough cylinder along beam direction when it emit Z bosons and quarkonium states, and the maximum velocity surface is a fat cylinder.

(c) The present work provides a reference in methodology which displays event patterns (scatter plots) for different particles in three-dimensional velocity space or other available spaces based on the transverse momentum and rapidity spectra of considered particles. It is expected that different particles correspond to rough cylinders with different diameters ($2\sqrt{\beta_x^2}$ or $2|\beta_x|_{\max}$) in velocity space. Our results show that the cylinders corresponding to emissions of charmonium $c\bar{c}$ mesons and bottomonium $b\bar{b}$ mesons are fatter than that of Z bosons, and the cylinders corresponding to the two quarkonium states are nearly the same.

Conflict of Interests

The authors declare that there is no conflict of interests regarding the publication of this paper.

Acknowledgments

This work was supported by the National Natural Science Foundation of China under Grant No. 11575103 and the US DOE under contract DE-FG02-87ER40331.A008.

References

- [1] L. Adamczyk, J. K. Adkins, G. Agakishiev et al. (STAR Collaboration), “Centrality dependence of identified particle elliptic flow in relativistic heavy ion collisions at $\sqrt{s_{NN}} = 7.7\text{--}62.4$ GeV,” *Physical Review C*, vol. 93, no. 1, Article ID 014907, 14 pages, 2016.
- [2] J. T. Mitchell for the PHENIX Collaboration, “The RHIC beam energy scan program: Results from the PHENIX experiment ,” *Proceedings of Science*, vol. CPOD 2013, Article ID 003, 10 pages, 2013, <http://arxiv.org/abs/1308.2185>.
- [3] J. Wilkinson for the ALICE Collaboration, “Mid-rapidity D-meson production in pp, Pb-Pb and p-Pb collisions at the LHC,” *Journal of Physics: Conference Series*, vol. 589, no. 1, Article ID 012020, 8 pages, 2015
- [4] S. Chatterjee, S. Das, L. Kumar, D. Mishra, B. Mohanty, R. Sahoo, and N. Sharma, “Freeze-out parameters in heavy-ion collisions at AGS, SPS, RHIC, and LHC energies,” *Advances in High Energy Physics*, vol. 2015, Article ID 349013, 20 pages, 2015.
- [5] N. Itoh, “Hydrostatic equilibrium of hypothetical quark stars,” *Progress in Theoretical Physics*, vol. 44, no. 1, pp. 291–292, 1970.
- [6] T. D. Lee and G. C. Wick, “Vacuum stability and vacuum excitation in a spin-0 field theory,” *Physical Review D*, vol. 9, no. 8, pp. 2291–2316, 1974.

- [7] Y.-H. Chen, G.-X. Zhang, and F.-H. Liu, “On productions of net-baryons in central Au-Au collisions at RHIC energies,” *Advances in High Energy Physics*, vol. 2015, Article ID 614090, 9 page, 2015.
- [8] F.-H. Liu, T. Tian, and X.-J. Wen, “Transverse mass and rapidity distributions and space dispersion plots of (net-)protons in Pb-Pb collisions at SPS energies,” *The European Physical Journal A*, vol. 50, no. 3, Article ID 50, 13 pages, 2014.
- [9] F.-H. Liu, “Dependence of charged particle pseudorapidity distributions on centrality and energy in p(d)A collisions at high energies,” *Physical Review C*, vol. 78, no. 1, Article ID 014902, 6 pages, 2008.
- [10] F.-H. Liu, “Unified description of multiplicity distributions of final-state particles produced in collisions at high energies,” *Nuclear Physics A*, vol. 810, nos. 1–4, pp. 159–172, 2008.
- [11] F.-H. Liu, Y.-Q. Gao, T. Tian, and B.-C. Li, “Unified description of transverse momentum spectrums contributed by soft and hard processes in high-energy nuclear collisions,” *The European Physical Journal A*, vol. 50, no. 6, Article ID 94, 9 pages, 2014.
- [12] L. D. Landau, “Izvestiya akademii nauk: series fizicheskikh 17 51 (1953),” in *English-Translation: Collected Papers of L. D. Landau*, D. Ter-Haarp, Ed., p. 569, Pergamon, Oxford, UK, 1965.
- [13] S. Z. Belenkij and L. D. Landau, “Soviet Physics Uspekhi 56 309 (1955),” in *English-Translation: Collected Papers of L.D. Landau*, D. Ter-Haarp, Ed., p. 665, Pergamon, Oxford, UK, 1965.
- [14] P. A. Steinberg, “Bulk dynamics in heavy ion collisions,” *Nuclear Physics A*, vol. 752, nos. 1–4, pp. 423–432, 2005.
- [15] P. Carruthers and M. Duong-Van, “Rapidity and angular distributions of charged secondaries according to the hydrodynamical model of particle production,” *Physical Review D*, vol. 8, no. 3, pp. 859–874, 1973.
- [16] E. V. Shuryak, “Multiparticle production in high energy particle collisions,” *Yadernaya Fizika*, vol. 16, no. 2, pp. 395–405, 1972.
- [17] P. Carruthers, “Heretical models of particle production,” *Annals of the New York Academy of Sciences*, vol. 229, no. 1, pp. 91–123, 1974.
- [18] O. V. Zhironov and E. V. Shuryak, “Multiple production of hadrons and predictions of the Landau theory,” *Yadernaya Fizika*, vol. 21, pp. 861–867, 1975.
- [19] M. Gazdzicki, M. Gorenstein, and P. Seyboth, “Onset of deconfinement in nucleus-nucleus collisions: review for pedestrians and experts,” *Acta Physica Polonica B*, vol. 42, no. 2, pp. 307–351, 2011.

- [20] Z. J. Jiang, H. P. Deng, Y. Zhang, and H. L. Zhang, “Unified descriptions of Hwa-Bjorken and Landau relativistic hydrodynamics and the pseudorapidity distributions in high energy heavy ion collisions,” *Nuclear Physics Review* (Chinese), In press.
- [21] S. Chatrchyan, V. Khachatryan, A.M. Sirunyan et al. (CMS Collaboration), “Study of Z production in PbPb and pp collisions at $\sqrt{s_{NN}} = 2.76$ TeV in the dimuon and dielectron decay channels,” *Journal of High Energy Physics*, vol. 2015, no. 3, Article ID 22, 40 pages, 2015.
- [22] V. Khachatryan, A. M. Sirunyan, A. Tumasyan et al. (CMS Collaboration), “Upsilon production cross section in pp collisions at $\sqrt{s} = 7$ TeV,” *Physical Review D*, vol. 83, no. 11, Article ID 112004, 27 pages, 2011.
- [23] S. Chatrchyan, V. Khachatryan, A. M. Sirunyan et al. (CMS Collaboration), “Measurement of the $\Upsilon(1S)$, $\Upsilon(2S)$, and $\Upsilon(3S)$ cross sections in pp collisions at $\sqrt{s} = 7$ TeV,” *Physics Letters B*, vol. 727, nos. 1–3, pp. 101–125, 2013.
- [24] B. Abelev, J. Adam, D. Adamová et al. (ALICE Collaboration), “Measurement of quarkonium production at forward rapidity in pp collisions at $\sqrt{s} = 7$ TeV,” *The European Physical Journal C*, vol. 74, no. 8, Article ID 2974, 21 pages, 2014.
- [25] K. Aamodt, A. A. Quintana, D. Adamová et al. (ALICE Collaboration), “Rapidity and transverse momentum dependence of inclusive J/ψ production in pp collisions at $\sqrt{s} = 7$ TeV,” *Physics Letters B*, vol. 704, no. 5, pp. 442–455, 2011.
- [26] K. Aamodt, A. A. Quintana, D. Adamová et al. (ALICE Collaboration), “Erratum to “Rapidity and transverse momentum dependence of inclusive J/ψ production in pp collisions at $\sqrt{s} = 7$ TeV” [Phys. Lett. B 704 (5) (2011) 442],” *Physics Letters B*, vol. 718, no. 2, pp. 692–698, 2012.
- [27] R. Aaij, B. Adeva, M. Adinolfi et al. (LHCb Collaboration), “Measurement of J/ψ production in pp collisions at $\sqrt{s} = 7$ TeV,” *The European Physical Journal C*, vol. 71, no. 5, Article ID 1645, 17 pages, 2011.
- [28] R. Aaij, C. A. Beteta, B. Adeva (LHCb Collaboration), “Measurement of $\psi(2S)$ meson production in pp collisions at $\sqrt{s} = 7$ TeV,” *The European Physical Journal C*, vol. 72, no. 8, Article ID 2100, 12 pages, 2012.
- [29] R. Aaij, C. A. Beteta, B. Adeva (LHCb Collaboration), “Measurement of Υ production in pp collisions at $\sqrt{s} = 7$ TeV,” *The European Physical Journal C*, vol. 72, no. 6, Article ID 2025, 12 pages, 2012.

Table 1. Values of free parameters (m_1 , $\langle p_{Ti} \rangle_1$, k_1 , m_2 , and $\langle p_{Ti} \rangle_2$), normalization constant (N_{p_T}), and χ^2/dof corresponding to the two-component Erlang distribution in Figures 1(a), 1(b), 2(a), 2(b), 5(a), 5(b) and 8(a).

Figure	Type	m_1	$\langle p_{Ti} \rangle_1$ (GeV/c)	k_1	m_2	$\langle p_{Ti} \rangle_2$ (GeV/c)	N_{p_T}	χ^2/dof
Figure 1(a)	$Z \rightarrow \mu\mu$	2	4.85 ± 0.20	0.78 ± 0.04	2	15.8 ± 0.79	55 ± 2.75	1.064
Figure 1(b)	$Z \rightarrow ee$	2	4.10 ± 0.20	0.60 ± 0.03	2	11.0 ± 0.55	63 ± 3.15	0.213
Figure 2(a)	$Z \rightarrow \mu\mu$	2	3.35 ± 0.17	0.45 ± 0.02	2	10.6 ± 0.53	$(3.57 \pm 0.18) \times 10^{-7}$	1.459
Figure 2(b)	$Z \rightarrow ee$	2	3.05 ± 0.15	0.54 ± 0.03	2	10.7 ± 0.53	$(3.85 \pm 0.19) \times 10^{-7}$	0.425
Figure 5(a)	J/ψ	2	1.15 ± 0.06	0.95 ± 0.04	2	2.34 ± 0.12	5 ± 0.25	1.416
Figure 5(b)	$\psi(2S)$	2	1.49 ± 0.07	0.82 ± 0.04	2	3.40 ± 0.17	0.39 ± 0.02	0.948
Figure 8(a)	$\Upsilon(1S)$	2	2.30 ± 0.12	0.65 ± 0.03	3	1.75 ± 0.09	2.38 ± 0.12	0.171
	$\Upsilon(2S)$	2	2.80 ± 0.14	0.32 ± 0.02	3	1.78 ± 0.09	0.56 ± 0.03	0.035
	$\Upsilon(3S)$	2	3.20 ± 0.16	0.60 ± 0.03	3	2.00 ± 0.10	0.29 ± 0.01	0.343

Table 2. Values of free parameter (σ_y), normalization constant (N_y), and χ^2/dof corresponding to the Gaussian distribution in Figures 1(c), 1(d), 2(c), 2(d), 5(c), 5(d), 8(b) and 9.

Figure	Type	σ_y	N_y	χ^2/dof
Figure 1(c)	$Z \rightarrow \mu\mu$	3.10 ± 0.16	510 ± 25	0.760
Figure 1(d)	$Z \rightarrow ee$	2.01 ± 0.10	370 ± 19	1.048
Figure 2(c)	$Z \rightarrow \mu\mu$	2.30 ± 0.12	2.35 ± 0.12	0.687
Figure 2(d)	$Z \rightarrow ee$	3.25 ± 0.16	3.50 ± 0.18	1.748
Figure 5(c)	J/ψ	3.15 ± 0.16	60 ± 3	0.755
Figure 5(d)	$\psi(2S)$	3.15 ± 0.16	10 ± 0.5	0.185
Figure 8(b)	$\Upsilon(1S)$	2.40 ± 0.12	13.5 ± 0.68	0.331
	$\Upsilon(2S)$	2.25 ± 0.11	3.3 ± 0.17	0.860
	$\Upsilon(3S)$	2.05 ± 0.10	1.8 ± 0.09	0.164
Figure 9(a)	$\Upsilon(1S)$	2.40 ± 0.12	518 ± 26	1.314
Figure 9(b)	$\Upsilon(2S)$	2.25 ± 0.11	168 ± 8	1.752

Table 3. Values of the root-mean-squares $\sqrt{p_T^2}$ for p_T and $\sqrt{y^2}$ for y corresponding to the particle scatter plots in Figures 3, 6, and 10.

Figure	Type	$\sqrt{p_T^2}$ (GeV/c)	$\sqrt{y^2}$
Figure 3(a)	$Z \rightarrow \mu\mu$	20.517 ± 1.026	3.004 ± 0.150
Figure 3(b)	$Z \rightarrow ee$	17.774 ± 0.889	1.942 ± 0.097
Figure 3(c)	$Z \rightarrow \mu\mu$	20.172 ± 1.009	2.260 ± 0.113
Figure 3(d)	$Z \rightarrow ee$	18.357 ± 0.918	3.396 ± 0.170
Figure 6(a)	J/ψ	3.102 ± 0.155	3.075 ± 0.154
Figure 6(b)	$\psi(2S)$	4.257 ± 0.213	3.192 ± 0.160
Figure 10(a)	$\Upsilon(1S)$	5.741 ± 0.287	2.332 ± 0.117
Figure 10(b)	$\Upsilon(2S)$	6.152 ± 0.308	2.320 ± 0.116
Figure 10(c)	$\Upsilon(3S)$	6.667 ± 0.333	1.106 ± 0.105

Table 4. Values of the root-mean-squares $\sqrt{\beta_x^2}$ for β_x , $\sqrt{\beta_y^2}$ for β_y , and $\sqrt{\beta_z^2}$ for β_z , as well as the maximum $|\beta_x|$, $|\beta_y|$, and $|\beta_z|$ ($|\beta_x|_{\text{max}}$, $|\beta_y|_{\text{max}}$, and $|\beta_z|_{\text{max}}$) corresponding to the particle scatter plots in Figures 4, 7, and 11.

Figure	Type	$\sqrt{\beta_x^2}$ (c)	$\sqrt{\beta_y^2}$ (c)	$\sqrt{\beta_z^2}$ (c)	$ \beta_x _{\text{max}}$ (c)	$ \beta_y _{\text{max}}$ (c)	$ \beta_z _{\text{max}}$ (c)
Figure 4(a)	$Z \rightarrow \mu\mu$	0.073 ± 0.004	0.071 ± 0.004	0.860 ± 0.043	0.598	0.545	1.000
Figure 4(b)	$Z \rightarrow ee$	0.078 ± 0.004	0.084 ± 0.004	0.791 ± 0.042	0.607	0.545	1.000
Figure 4(c)	$Z \rightarrow \mu\mu$	0.087 ± 0.004	0.090 ± 0.005	0.800 ± 0.040	0.441	0.529	1.000
Figure 4(d)	$Z \rightarrow ee$	0.061 ± 0.003	0.062 ± 0.003	0.864 ± 0.043	0.584	0.397	1.000
Figure 7(a)	J/ψ	0.191 ± 0.010	0.195 ± 0.010	0.866 ± 0.043	0.760	0.830	1.000
Figure 7(b)	$\psi(2S)$	0.189 ± 0.009	0.190 ± 0.009	0.865 ± 0.043	0.878	0.822	1.000
Figure 11(a)	$\Upsilon(1S)$	0.156 ± 0.008	0.154 ± 0.008	0.804 ± 0.040	0.781	0.745	1.000
Figure 11(b)	$\Upsilon(2S)$	0.147 ± 0.007	0.141 ± 0.007	0.795 ± 0.040	0.719	0.678	1.000
Figure 11(c)	$\Upsilon(3S)$	0.206 ± 0.010	0.213 ± 0.011	0.793 ± 0.040	0.785	0.754	1.000

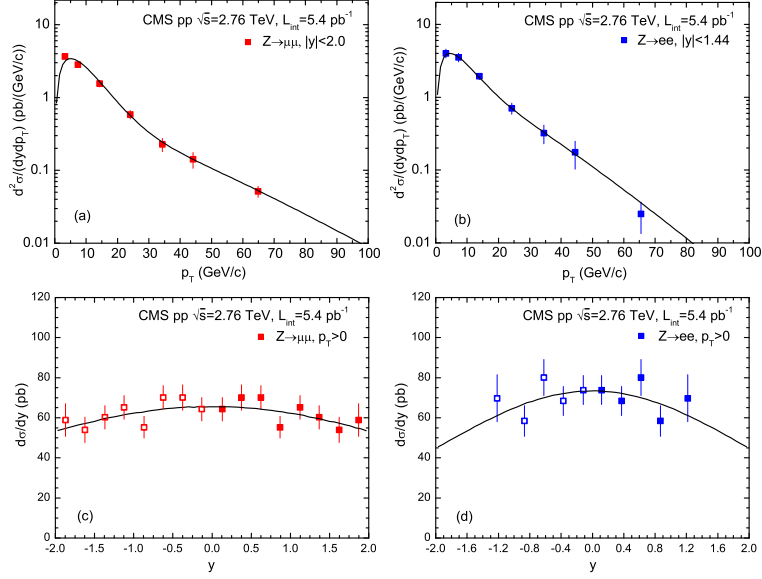


Fig. 1. (a)(b) Transverse momentum spectra and (c)(d) rapidity spectra of Z bosons produced in pp collisions at $\sqrt{s} = 2.76$ TeV, for the (a)(c) dimuon ($\mu\mu$) and (b)(d) dielectron (ee) decay channels. The solid squares represent the experimental data of the CMS Collaboration [21], and the open squares are reflected at $y = 0$. The curves are our results calculated by using the (a)(b) two-component Erlang distribution and (c)(d) Gaussian distribution, respectively.

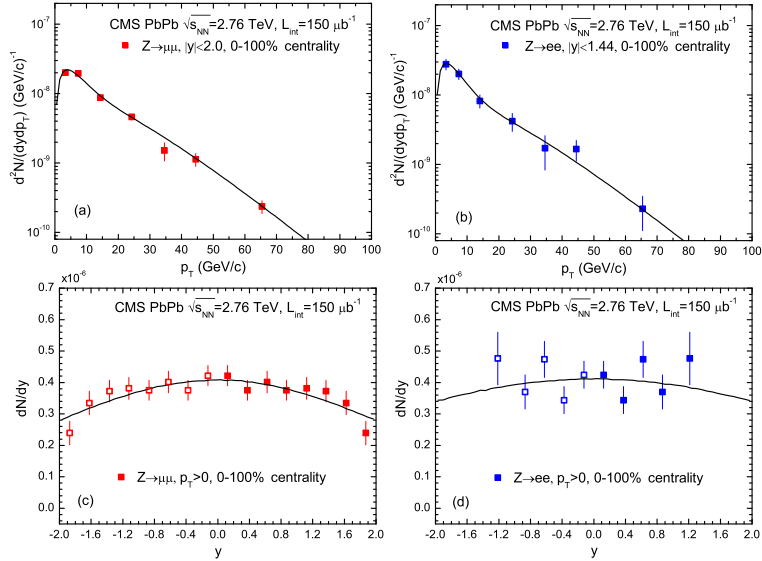


Fig. 2. Same as Figure 1, but showing the results in minimum-bias Pb-Pb collisions at $\sqrt{s_{NN}} = 2.76$ TeV.

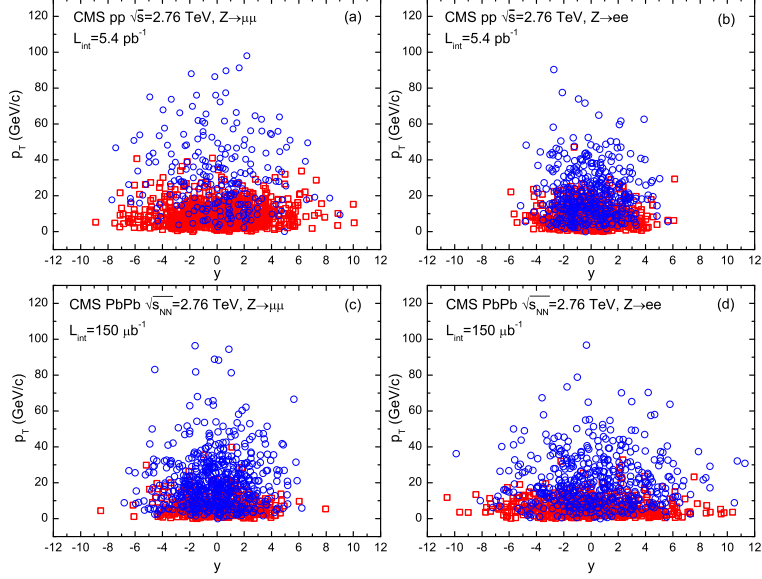


Fig. 3. Event patterns (particle scatter plots) in two-dimensional $p_T - y$ space in (a)(b) pp collisions at $\sqrt{s} = 2.76$ TeV and (c)(d) Pb-Pb collisions at $\sqrt{s_{NN}} = 2.76$ TeV, for the (a)(c) dimuon and (b)(d) dielectron decay channels. The number of Z bosons for each panel is 1000. The squares and circles represent the results of the first and second components in the two-component Erlang distribution, respectively.

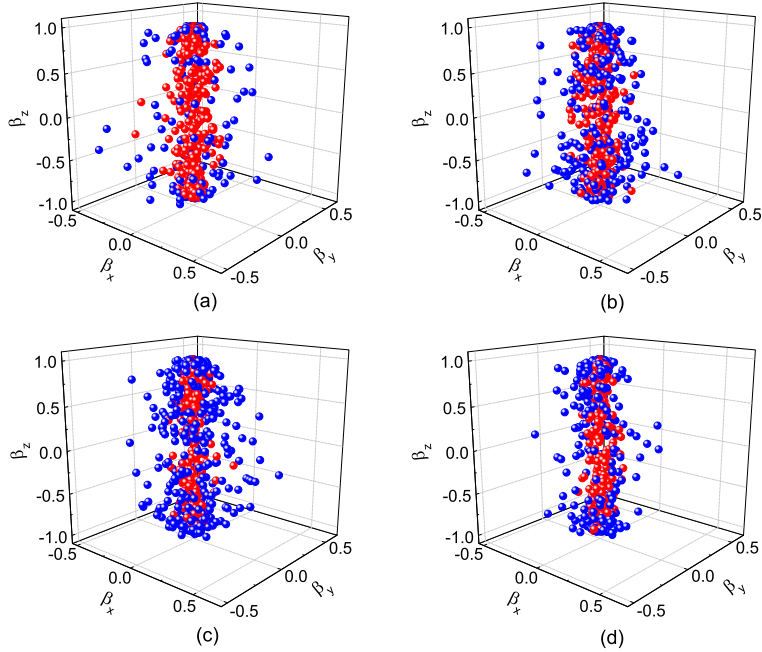


Fig. 4. Event patterns in three-dimensional velocity ($\beta_x - \beta_y - \beta_z$) space in (a)(b) pp collisions at $\sqrt{s} = 2.76$ TeV and (c)(d) Pb-Pb collisions at $\sqrt{s_{NN}} = 2.76$ TeV, for the (a)(c) dimuon and (b)(d) dielectron decay channels. The number of Z bosons for each panel is 1000. The red and blue globules represent the results of the first and second components in the two-component Erlang distribution, respectively.

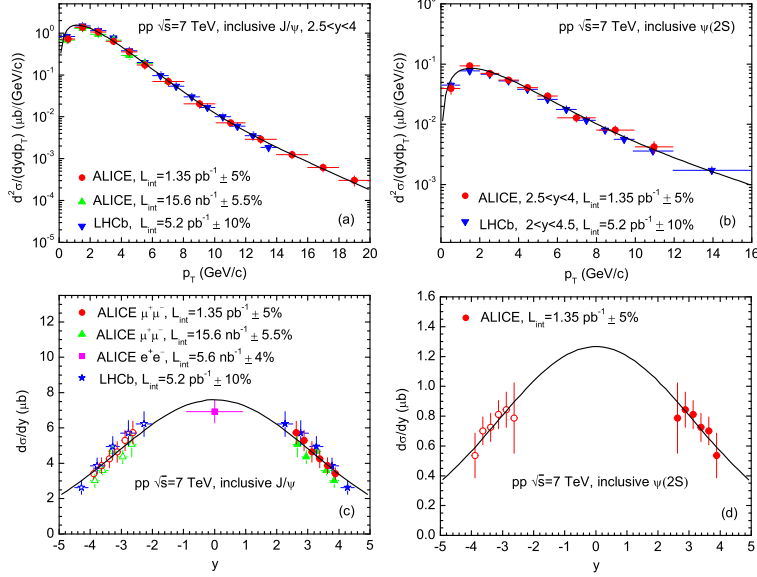


Fig. 5. (a)(b) Transverse momentum spectra and (c)(d) rapidity spectra of (a)(c) J/ψ mesons and (b)(d) $\psi(2S)$ mesons produced in pp collisions at $\sqrt{s} = 7$ TeV. The solid symbols represent the experimental data of the ALICE [24–26] and LHCb Collaboration [27, 28], and the open symbols are reflected at $y = 0$. The curves are our results calculated by using the hybrid model.

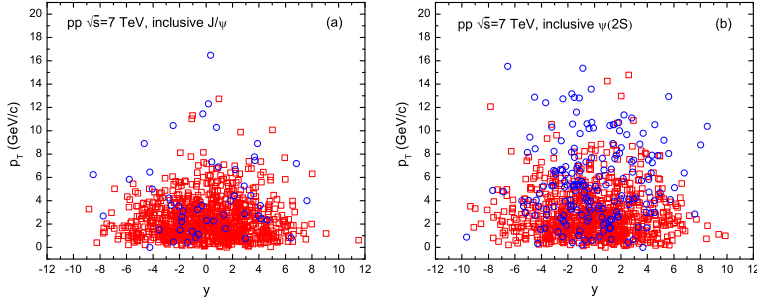


Fig. 6. Same as Figure 3, but showing the results for (a) J/ψ mesons and (b) $\psi(2S)$ mesons produced in pp collisions at $\sqrt{s} = 7$ TeV.

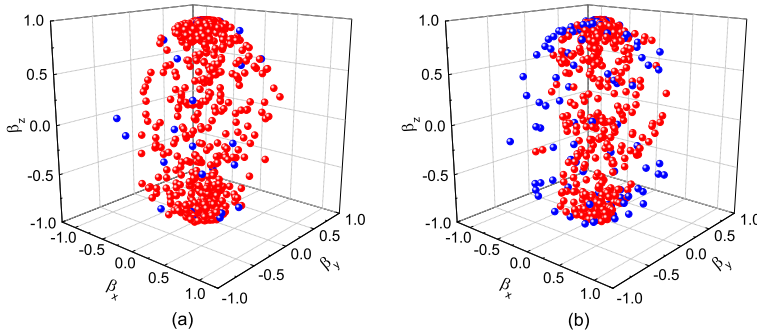


Fig. 7. Same as Figure 4, but showing the results for (a) J/ψ mesons and (b) $\psi(2S)$ mesons produced in pp collisions at $\sqrt{s} = 7$ TeV.

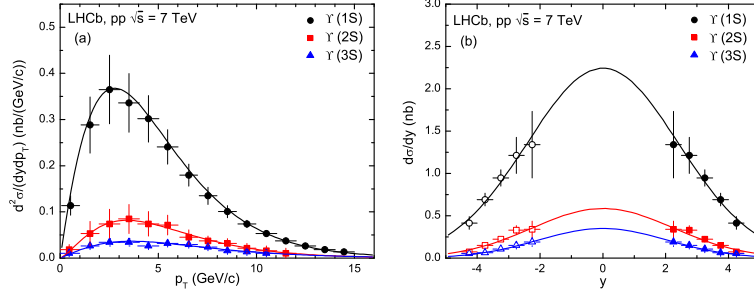


Fig. 8. (a) Transverse momentum spectra and (b) rapidity spectra of bottomonium $b\bar{b}$ mesons $\Upsilon(1S)$, $\Upsilon(2S)$, and $\Upsilon(3S)$ produced in pp collisions at $\sqrt{s} = 7$ TeV. The solid symbols represent the experimental data of the LHCb Collaboration [29], and the open symbols are reflected at $y = 0$. The curves are our results calculated by using the hybrid model.

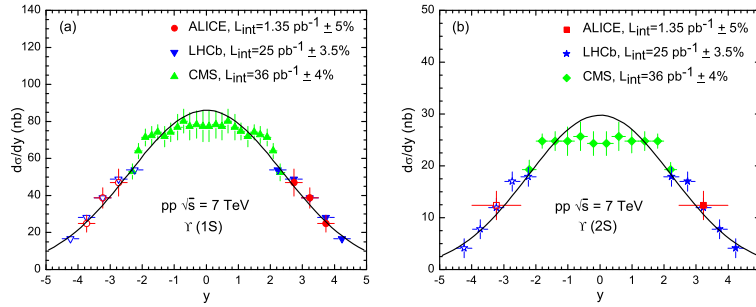


Fig. 9. Rapidity spectra of (a) $\Upsilon(1S)$ and (b) $\Upsilon(2S)$ mesons produced in pp collisions at $\sqrt{s} = 7$ TeV. The solid symbols represent the experimental data of the ALICE [24], LHCb [29], and CMS Collaborations [22, 23], and the open symbols are reflected at $y = 0$. The curves are our results calculated by using the hybrid model.

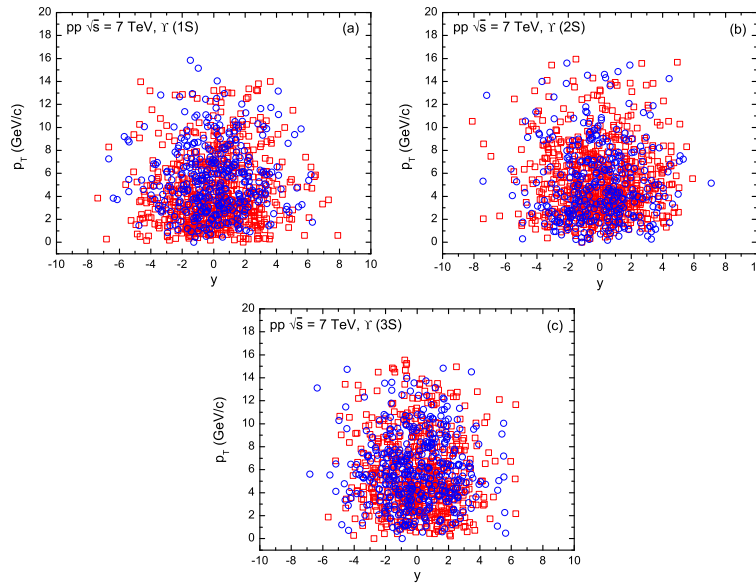


Fig. 10. Same as Figure 3, but showing the results for (a) $\Upsilon(1S)$, (b) $\Upsilon(2S)$, and (c) $\Upsilon(3S)$ mesons produced in pp collisions at $\sqrt{s} = 7$ TeV.

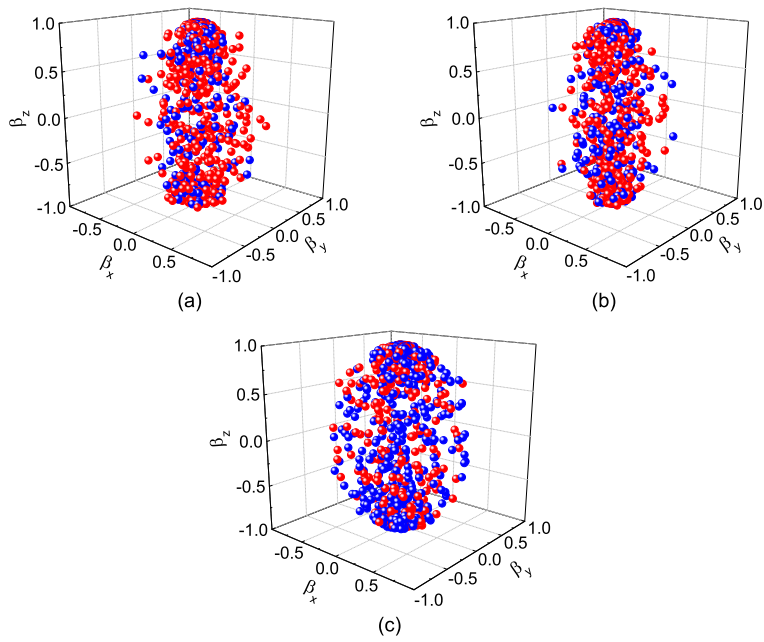


Fig. 11. Same as Figure 4, but showing the results for (a) $\Upsilon(1S)$, (b) $\Upsilon(2S)$, and (c) $\Upsilon(3S)$ mesons produced in pp collisions at $\sqrt{s} = 7$ TeV.